Polymer-Based Wide-Bandwidth and High-Sensitivity Micromachined Electron Tunneling Accelerometers Using Hot Embossing

Tianhong Cui, *Senior Member, IEEE,* and Jing Wang

***Abstract*—The first PMMA-based membrane tunneling accelerometers were fabricated by hot embossing replication with silicon molds. The silicon molds were prepared by a combinative etching technique involving anisotropic bulk etching and modified plasma dry etching. The constructed molds hold both pyramid pits and positive profile sidewalls with smooth surfaces and steep angles, which were necessary for the hot embossing demolding. After electrodes patterned on embossed PMMA structures, the accelerometers, 8 mm × 8 mm × 1 mm, were packaged and assembled on a measurement circuit board. The exponential relationship between tip currents and applied deflection voltages presented a tunneling barrier height of 0.17 eV. The natural frequency of sensors was about 128 Hz. The bandwidth of the feedback system was 6.3 kHz. The sensitivity of voltage over acceleration was 20.6 V/g, and the resolution was 0.2485 $\mu g/\sqrt{\text{Hz}}$ ($g = 9.8\ \text{m/s}^2$). [1349]**

***Index Terms*—Accelerometer, electron tunneling, hot embossing, MEMS, PMMA.**

I. Introduction

In 1986 the Nobel Prize was awarded to Binnig and Rohrer for the first scanning tunneling microscope (STM). Since then, the possibility of making highly sensitive tunneling displacement transducers utilizing the electron tunneling effect has been actively explored. Several years after the advent of the first tunneling transducer [1], sensors with a displacement resolution approaching $10^{-4}\ \text{Å}/\sqrt{\text{Hz}}$ were developed by Waltman [2] and Kenny [3], respectively.

In electron tunneling transducers, subangstrom changes in displacement will induce measurable changes in tunneling current. This high sensitivity is independent of the lateral size of the electrodes because the tunneling current occurs between two metal atoms located at the opposite electrode surfaces [4]–[7]. Moreover, the tunneling current exponentially increases with the displacement changes, thus the tunneling sensors excel most of the existing sensors with piezoelectric, capacitive, piezoresistive, or interferential principles. Due to their high sensitivity and small size, the micromachined tunneling transducers make it possible to fabricate sensors with the advantages such as high performances (both in sensitivity and resolution), miniature size, and low cost. The tunneling effect has been an attractive technology for accelerometer instrumentation with great demands in the applications to microgravity measurement, acoustic measurement, seismology, and navigation.

In recent years, some new materials and micromachining tools have been widely used in Microelectromechanical Systems (MEMS). PMMA, as a type of elastomer, has drawn a lot of attention for soft lithography, microfabrication, and nanomanufacturing. The reasons are the following. The price of PMMA sheets is about $0.10 per square inch, ten times less than silicon wafers. The bonding temperature of PMMA is about 150 °C, much lower than silicon. Owing to the elastic properties, it is easier to seal the interfaces between surfaces and to fabricate the materials. The biocompatibility of PMMA will make it suitable for a lot of biomedical or biological applications in the future.

On the other hand, hot embossing has been widely used in many applications by exploiting the thermoplastic properties of PMMA. Due to the characteristics such as insulation, biocompatibility, and transparency, PMMA has been used to build microstructures such as microfluidic channels [8], chemical nano patterns [9], and optical gratings [10], [11]. The hot embossing technique with the advantages of quick processing and mass fabrication is also employed. Due to the repeatable use of templates in hot embossing, the cost of mold fabrication can be neglected in the entire processing. The replication of microstructures from templates to PMMA makes it a real mass-production process. The whole processing time for such a replication can be less than 20 min, much quicker than the silicon processing. The roughness of the embossed surface can be only 3.9 nm [12], which can compete with any polished silicon surface, and the surface smoothness can be kept in good uniformity throughout the entire wafer area. The lateral resolution of hot embossing can reach several nanometers [13]. Actually there is no limitation of lateral feature sizes for this technique. The limitation of line width comes from the availability of the molds themselves. Furthermore, the hot embossing is a one-step process, and it consumes much less chemicals and needs fewer instruments involved.

The objective of this work is to use polymer, instead of silicon, to fabricate an inexpensive, batch-produced, and highly sensitive tunneling sensor platform. The first step of this project is to realize a one-dimensional (1-D) vertical device (sensitive to

Manuscript received May 24, 2004; revised January 10, 2005. This work is partially supported by grants NSF/LEQSF (2001-04)-RII-02, DARPA DAAD19-02-1-0338, and NASA (2002)-Stennis-22. The experimental work was implemented at the Institute for Micromanufacturing, Louisiana Tech University, Ruston, LA 71272 USA. Subject Editor T. Kenny.

T. Cui is with Department of Mechanical Engineering and Nanofabrication Center, University of Minnesota, Minneapolis, MN 55455 USA (e-mail: tcui@me.umn.edu).

J. Wang is with Department of Mechanical Engineering and Applied Mechanics, University of Pennsylvania, Philadelphia, PA 19104 USA.

Digital Object Identifier 10.1109/JMEMS.2005.851865

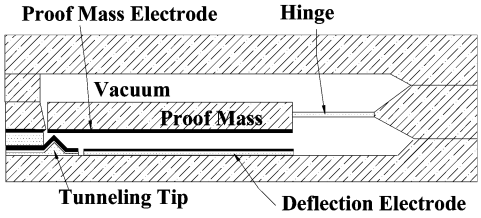

Fig. 1. Cross section schematic of a micromachined tunneling accelerometer with a cantilever structure.

the z-axis normal to the wafer surface). The ultimate goal is to obtain a 3-D microsensor platform for variety of applications. Once the polymer sensor platform is implemented, five application areas will be considered to take advantage of the potential of this advanced MEMS technology. The five applications include accelerometer, chemical sensor, infrared (IR) radiation sensor, displacement sensor, and magnetic sensor. This paper reports the PMMA-based tunneling sensor functioning as an accelerometer, which is the first structure under consideration.

II. Operation Principle

A typical tunneling accelerometer has mechanical components and three electrodes. A cross section of the tunneling accelerometer with a cantilever structure is illustrated in Fig. 1. The mechanical components comprise of a fixed cantilever with a tunneling tip on the bottom and a mass component, or a poof mass, suspended by a flexible hinge on the top. The electrodes include a tip electrode, a counter electrode under the proof mass, and a deflection electrode. Gold is chosen as the electrode metal due to its inert chemical characteristics as well as its relatively high work function. When operating in a closed-loop mode, the accelerometer maintains a constant tip-to-proof mass distance by applying an electrostatistic feedback force on the proof mass.

The metal tip and the counter electrode construct a tunneling junction. Usually the biased voltage of the junction is about 250 mV. In the constant-distance mode, the gap between the tip and the proof mass is about 10 Å, and the tunneling current is about 1.5 nA. The tunneling current, I, varies exponentially with the gap change, s [Å]. The formula is written as

$$I = I_o \exp(-\alpha s\sqrt{\Phi}) \tag{1}$$

where Φ [eV] is the height of the tunneling barrier, I_o is the original tunneling current, and α is the constant of 1.025 [$\text{Å}^{-1}\text{eV}^{-1/2}$]. It can be derived that

$$\text{const} = \frac{d\ln I}{ds} \tag{2}$$

which means that the exponential relationship between the tunneling current and the separation gap can be obtained by measuring the slope of the semilog plot of tunneling currents versus gap changes. Equation (2) is useful when affirming tunneling effect and feedback control in closed-loop measurements. More detailed descriptions about tunneling structures and operation principles can be found in [14], [15].

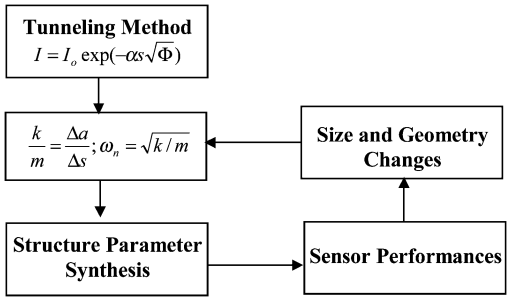

Fig. 2. Design flow chart of the accelerometer. Force balance indicates the k/m ratio, which relates to both the sensitivity and the natural frequency. Furthermore, the k/m ratio determines the structure parameters and sensor performances. After checking the sensor characteristics, the size and geometry of sensor structures are revised, which in turn, resulting in a new k/m ratio.

III. Structure and Controller Design

A. Design Principle

The design flow chart of the accelerometer is shown in Fig. 2. Under force balance, there exists

$$k\Delta s = m\Delta a \tag{3}$$

where m and k are mass and stiffness of the proof mass, respectively. The k/m ratio is very important because it is inversely proportional to the displacement sensitivity, $\Delta s/\Delta a$. The ratio also describes the natural frequency of proof mass by $\omega_n = \sqrt{K/m}$. It is easier to measure the natural frequency, and we can always arbitrarily choose the proof mass to satisfy the requirements for the k/m ratio. Therefore, the design of the tunneling accelerometer can start with the choice of k/m ratio. To exhibit fast response time and large bandwidth, a higher k/m ratio is necessary so that accelerometers can have high natural frequencies. However, for high sensitivity and good resolution, a small k/m ratio is required. Moreover, a smaller k/m ratio gives rise to smaller noise level because the expected noise source is given by:

$$N_{\text{thermal}} = \sqrt{\frac{4k_B T\omega_o}{m_p Q}} \tag{4}$$

where k_B is the Boltzmann constant, T is the temperature in Kelvin, ω_o is the resonant frequency of the structure, m_{P} is the proof mass, and Q is the laden quality factor [16]. Therefore, the choice of k/m ratio is competitive and compromised. An experiential value is chosen so that the natural frequency is about 100 Hz. The k value also determines the mechanical structures and sizes, which can be synthesized either by a mathematical method for simple structures or by a simulation method aided by ANSYS or other finite element analysis (FEA) softwares. Other properties, such as the open-loop characteristics and actuator performances, can also be predicted. The designed properties are inspected with control and feedback systems, which mainly determine the whole system performances.

The most challenging task for a tunneling accelerometer design is to enhance the resolution while broadening the frequency bandwidth. Liu, *et al.* developed a controller design by μ-synthesis [17], which accomplished a high-precision, wide-bandwidth, and micromachined tunneling accelerometer

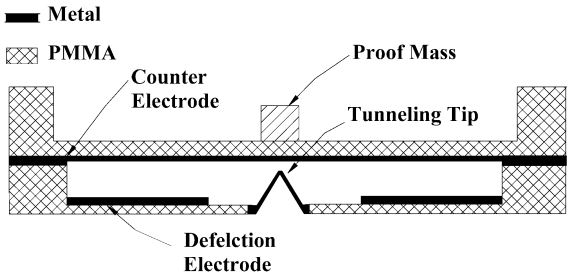

Fig. 3. Micromachined accelerometer with a membrane structure. The sensitive direction is normal to the membrane surface.

[18]. Partridge, *et al.* utilized diode self-actuation for temperature compensation, presented an integrated, and completed tunnelling sensor controller [19]. Recently, a simple design method was established by the aid of approximation at small signal input in our group [20]. With this properly designed feedback circuit, together with parameter changes and an electrostatic actuator, a closed-loop system was obtained. Finally, the accelerometer was characterized with a gravimeter.

B. Manufacturing Design

There are mainly two types of tunneling accelerometer structures: cantilever structures and membrane structures. The main advantage of the cantilever tunneling structure is the large linear range. However, operating in the constant-distance mode, the gap variation is less than 1 Å, which is rather small. In addition, the membrane structure is more suitable for the hot embossing process. Thus, the intended z-direction sensitive tunneling sensors adopt the membrane structure [21], as illustrated in Fig. 3.

The narrow gap between the tunneling tip and the counter electrode is about 10 Å when the tunneling sensor is functional. It is difficult to realize such a small distance without the aid of deflection electrodes acting as a capacitive actuator, which not only pull down the counter electrode membrane to the proper position, but also produce feedback static forces to keep the distance constant. The thickness of membrane, the original gap between the counter electrode and the tunneling tip, and the static force distribution were simulated with ANSYS before the fabrication. Because the Young's modulus of PMMA is 3.9 GPa, about 2/9 of silicon's value of 179 GPa [22], the PMMA is rather softer than silicon. Therefore, the thickness of membrane could be thicker than a silicon structure, which is another reason why all-PMMA structures are easier to fabricate. The designed dimensions of the device were from ANSYS static analysis. The spring constant k changes dramatically when either the sheet parameter or the proof mass changes. However, the main condition to determine the k value is the sheet sizes in magnitude scale, while the proof mass only changes one to two times. A well synthesized PMMA tunneling accelerometer includes a membrane 50 μm thick and 2 mm $\times$ 2 mm in lateral dimensions, a pyramid tunneling tip 50 μm high and 70 μm in base lines, and a square proof mass of 100 μm$\times$ 100 μm with a flexible height.

C. Feedback and Control System Synthesis

Considerable research work on accelerometers [23]–[25] has been reported. However, most micromachined tunneling accelerometers still suffer the problem of enhancing resolution while broadening measurement bandwidth. For new device designers, who intend either to develop innovative tunneling sensors or to reconstruct revised structures for better performances, a simple and effective design method is necessary. A Computer Aided Engineering (CAE) tool, MatLab Simulink, has been chosen to model and simulate the function of the tunneling accelerometer. The distance change between the tunneling tip and the proof mass, Δs, which had been measured by a laser vibration measurement system as 10^{-3} to 10^{-1} Å [14], was rather small, compared with the normal operation position of 10 Å. Therefore, the tunneling current could be developed by Taylor Series. The nonlinear system changed into a linear system at wavelet analysis. The open-loop and closed-loop transfer functions of whole system H_o and H are

$$\begin{cases} H_o = H_c \cdot H' \\ H = \frac{H_o}{1+FH_o} \end{cases} \tag{5}$$

where H_c is the control circuit transfer function, H' is the linear relation of system, and F is the feedback factor.

From the above analysis, the system properties were synthesized by choosing a control and feedback system. By choosing a designed control system, the accelerometer bandwidth was broadened and the damping was enhanced. The system stability, root locus, step response, gain and phase margin, and pole-zero distribution were all inspected. With the designed control and feedback system, a closed-loop system was stable on both parameter disturbance and frequency response. The tunneling accelerometer characteristics, such as exponential relationship between tunneling current and displacement change, time history record, dynamics and frequency response were also presented. The detailed description was reported in [20].

IV. Device Fabrication

The structures of PMMA-based tunneling sensors were fabricated by the hot embossing technique. The fabrication started from a silicon template. The hot embossing was performed to produce PMMA embossed sheet, followed by the electrode metal films deposited and patterned. After assembly and package, the accelerometers were ready for detection.

A. Combinative Etching for Silicon Molds

Currently, there are mainly three types of methods to build hot embossing templates. The first one is wet anisotropic etching, which is simple, but has low aspect ratio. The second one is plasma deep reactive etching (DRIE). DRIE can accomplish silicon molds with high aspect ratios, but needs to be well controlled so that the tapered sidewalls are smooth and positive, which is necessary to avoid cracking at hot embossing demolding. The last approach is electroplating of Nickel with the aid of photolithography and a seed layer. However, the electroplating processing is complicated, slow, and the conditions for profile control are tricky. As shown in Fig. 3, the tunneling transducer includes different parts such as a tunneling pyramid, which has a sharp tip for tunneling currents, and some blocks with steep and high-aspect ratio sidewalls. In the meantime, the height of a proof mass needs to be changed from chip to chip so that the parameters of transducers can be adjusted promptly.

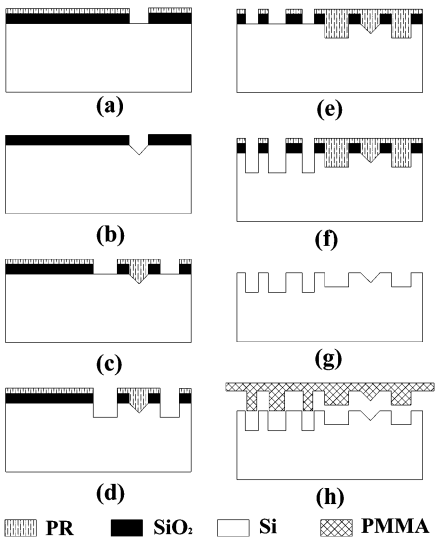

Fig. 4. Combinative technique to fabricate silicon master for hot embossing. In step (a), SiO_2 is patterned by photolithography. In step (b), pyramid pit is obtained by KOH anisotropic etching with SiO_2 as a mask. In step (c), the second SiO_2 mask pattern is prepared for the ICP etching. In step (d), modified ICP etching is performed to obtain the high-aspect-ratio parts in the silicon master. In step (e), the pyramid part of silicon mold is protected and SiO_2 is patterned by BOE. In step (f), modified ICP etching is performed to get deep proof mass structure. In step (g), the mold is finally fabricated after cleaning. In step (h), the structure is transferred to PMMA by hot embossing.

Consequently, it is hard to obtain a single hot-embossing template only by the conventional process. A combination of KOH (potassium hydroxide) wet etching and plasma etching were used to construct the silicon templates so that the requirements for different parts can be met.

The fabrication of silicon templates for hot embossing started with KOH wet etching. Silicon dioxide was selected as an etching mask. As shown in Fig. 4(a), SiO_2 was patterned by a positive photoresist (PR1813), and etched with diluted BOE. The etching rate was well controlled at a relative slow rate of 800 $\text{Å}/\text{min}$. After that, the photoresist was removed with acetone, and the whole wafer was soaked into a 45% KOH etchant. The etchant was kept at 85°C with a stirrer rotating at 200 RPM. The etching time was about 60 minutes with an etching rate of 1 μm per minute [Fig. 4(b)]. Another buffered HF etching was performed after the second photolithography [Fig. 4(c)]. The deep pyramid pits were protected thoroughly for the following plasma etching. The normally used high-density plasma, SF_6 and O_2, results in an isotropic undercut profile. This undercut is unsuitable for hot embossing, since it causes either the cracking of silicon templates or the damage of PMMA structures at demolding. ICP (Inductive Coupled Plasma) Bosch etching, in which the gases switch between SF_6/O_2 and C_4F_8, did not work in the case because a rather rough surface ("grass") was observed in the large etched areas [26], though it could achieve a positive taper profile. In Fig. 4(d), a modified process was carried out, in which SF_6, O_2, and C_4F_8 were used simultaneously to acquire the positive sidewall profiles and smooth surfaces. After the ICP etching, the wafer was cleaned, and another photolithography was implemented [see Fig. 4(e)]. The photoresist was relatively thicker since this time the second plasma etched thickness was about 80 to 100 μm [see Fig. 4(f)]. Subsequently, the thermal oxide was removed, and the silicon

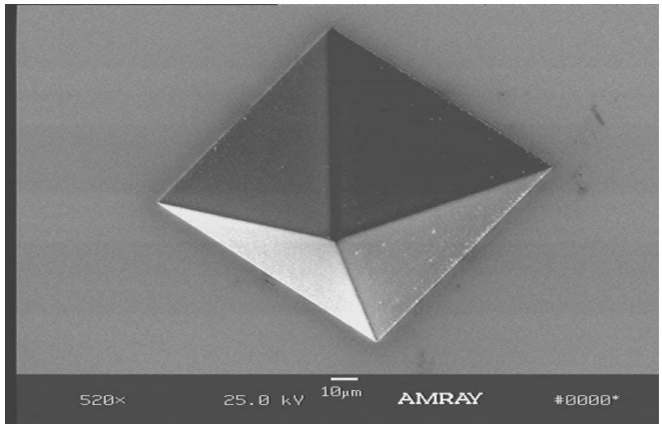

Fig. 5. Pyramid structure with sharp edges in silicon master produced by modified etching method. The tip is 50 μm in depth and 70 μm in each side.

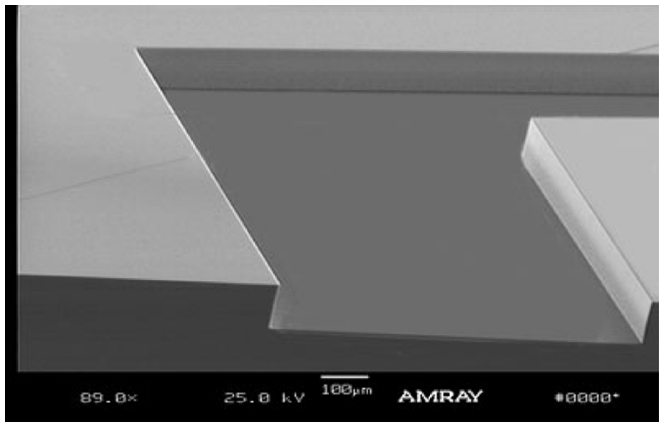

Fig. 6. Proof mass in a silicon master using optimized plasma etching. The master has positive sidewall profile, smooth surface,and sharp edges.

template was thoroughly cleaned [see Fig. 4(g)], followed by anodic bonding to a 5 mm thick Pyrex glass wafer. The hot embossing was executed, and the structures were replicated into PMMA [see Fig. 4(h)]. A SEM picture of a silicon pit on mold is shown in Fig. 5, in which the sidewall of the pyramid is smooth and the four edges are sharp.

As described above, three gases, SF_6, O_2, and C_4F_8, resulted in both isotropic chemical etching and anisotropic physical etching during the plasma etching. The positive and smooth sidewalls, shown in Fig. 6, were obtained by optimizing the flowrates as 200 sccm SF_6, 20 sccm O_2 at 100 W (ICP), 20 W (bias), a working pressure of 60 mTorr, and a temperature of 10 °C.

B. Structure Replication With Hot Embossing

During hot embossing for a structure replication, a polymer plate was laid on the bottom heating plate of the hot embossing machine, and the surrounding vacuum chamber was closed. Under vacuum, the heated mold was pressed into the softened polymer. After subsequent cooling, the demolding was implemented by removing the plastic part from the mold cavities. According to the data in [27], the glass transaction temperature of PMMA is about 100–105 °C, and the melting temperature is about 112–130 °C. The molding temperature was set at 165 °C, higher than the melting temperature in case

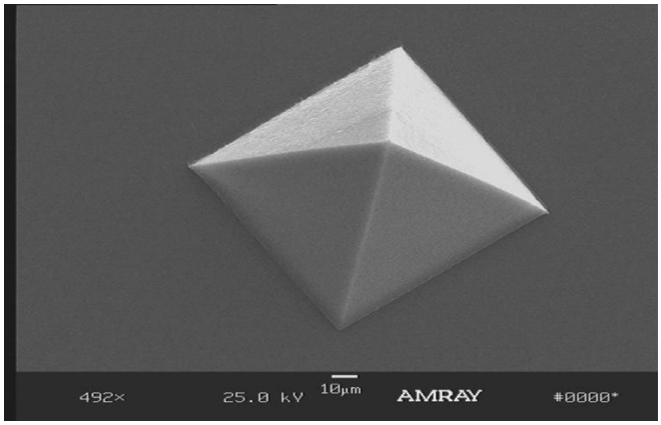

Fig. 7. SEM picture of a PMMA tunneling tip embossed by hot embossing replication. The tip has smooth surfaces, sharp edges, and square base lines the same as the silicon master.

of uncertainty. During molding, the chamber was compressed down, with a maximum contact force of 20 kN. The background pressure was about 1.5 mbar. The template was maintained for about 60 seconds before it began to cool down. The demolding system was designed to overcome the holding force between tool and PMMA with the aid of a pressurized air applied from the top of the template holder. In our case, the demolding temperature was set at 80 °C. The speed of moving mold is 1 mm/min. The fabricated PMMA pyramids, shown in Fig. 7, have smooth surfaces, sharp tip points, and steep edges.

The PMMA was then sliced into two parts. In order to get better adhesion, there was a layer of Ti (titanium) film deposited before gold sputtering. The electrodes were patterned by two steps of standard wet etching. Gold etchant, I_2: KI: H_2O = 1:5:50 (weight), produced an etching rate of 300 $\text{Å}/\min$, and BOE etched a 200 Angstroms Ti film within a few seconds.

C. Assembly and Package

After wire-electrode connection and the two parts of the PMMA structures glued together by an electrical conductive glue, the devices were fixed onto an 18-pin socket. The assembly was manipulated manually with the aid of a stereomicroscope. The photographs of three packed sensors are shown in Fig. 8(b), where an electrode with a patterned bottom part is also illustrated in Fig. 8(a).

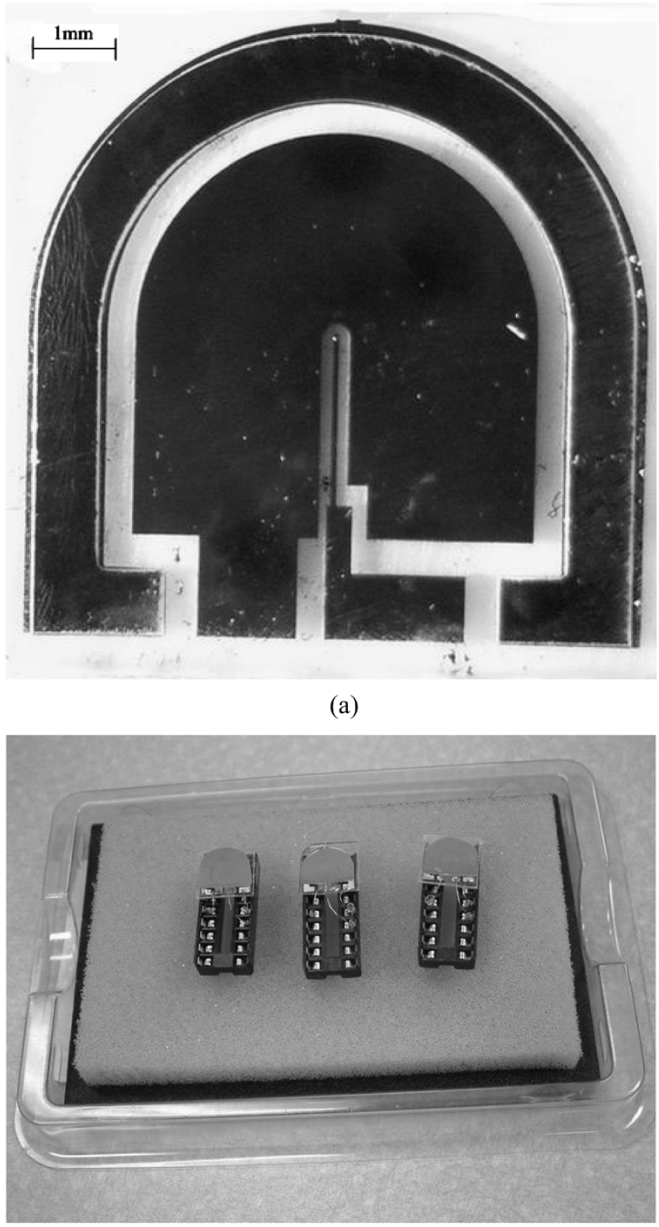

(a)

(b)

Fig. 8. (a) Illustration of an electrode-patterned device and (b) packed PMMA membrane tunneling sensors.

V. Device Characterization

A. The Properties of Mechanical Structures

The main properties of mechanical structures include the vibration amplitude and the vibration frequency response. The natural frequency of the membrane is measured when the packed tunneling sensors were glued onto the vibration exciter. The vibration force was kept constant, while the exciter's frequency changed. The induced vibration amplitude was measured with Polytec Laser Vibrometer VDD 650.

The plot of vibration frequency responses of a PMMA tunneling sensor is shown in Fig. 9. The response is measured at an exciter acceleration of 1 mg. The sharp peak corresponds to the natural frequency of 128 Hz. Compared with the designed value of 100 Hz, the difference may result from the uncertainty of membrane thickness, which could range from 50 to 80 μm instead of a designed value of 50 μm. The variation of membrane thickness resulted in the natural frequency variation of $\pm 15\%$ in seven different accelerometers.

B. Open Loop Properties

When a tunneling accelerometer operated in open loop status, the tunneling current was characterized. A high dc voltage was applied on the deflection electrode, which set the gap between the tunneling tip and the counter electrode to a proper value of 1 nm. Next, an ac voltage with a frequency lower than the natural frequency f_o was applied to the deflection electrode. The inspired force produced a small vibration of the proof mass. An ac current I_t was induced on the tunneling tip, which had relation with both the high dc voltage and the ac deflection voltage.

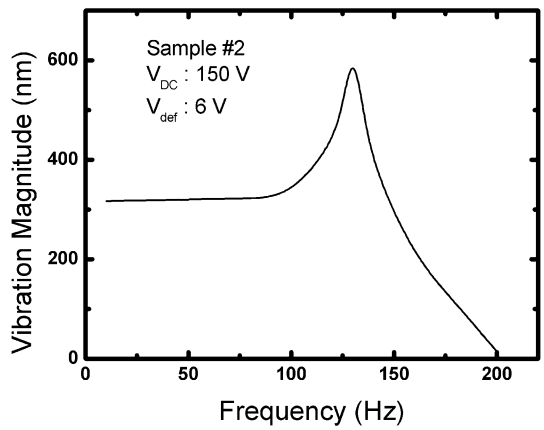

Fig. 9. vibration responses versus frequencies of a PMMA tunneling sensor. The response is measured at an exciter acceleration of 1 mg. The sharp peak corresponds to the natural frequency of $f_o = 128$ Hz, a little higher than the designed value of 100 Hz.

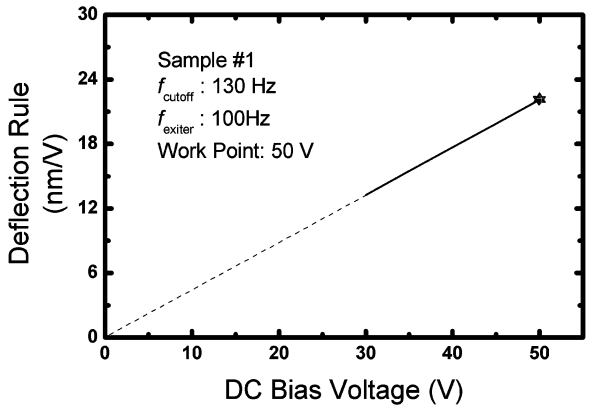

Fig. 11. The illustration of static actuator deflection rule. The ratios of vibration amplitudes over ac deflection voltages are plot at different high dc voltage biases. The frequency of the deflection voltages was chosen as 100 Hz, less than its natural frequency 130 Hz. The value marked as asterisk is the intended working point thereafter.

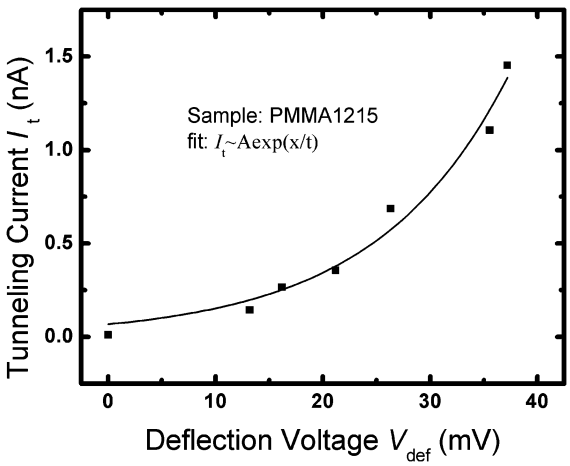

Fig. 10. The illustration of tunneling current versus deflection ac voltage. The curve demonstrates the exponential relationship, verifying the electron tunneling effect.

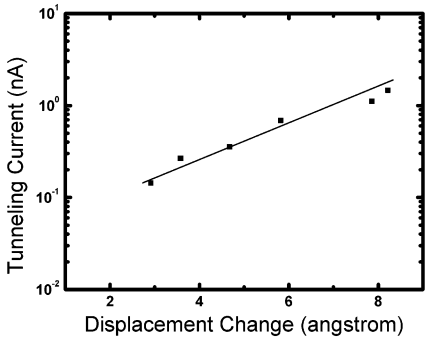

Fig. 12. The semilog plot of tunneling current versus displacement change. The effective barrier height $\Phi = 0.1685$ eV is obtained according to the formula $I = I_o \exp(-\alpha s\sqrt{\Phi})$.

The measured curve of deflection ac voltages and tunneling tip currents is plotted in Fig. 10. The curve demonstrated that there is an exponential relationship between the deflection voltage and the tunneling current when the dc voltage is constant.

As analysis in [28], the deflection voltage is linearly proportional to the tip movement because the DC voltage is much higher than the ac voltage on deflection electrode, though the capacitive actuator has a reciprocal square law between the gap and the voltage. The measurement of this relation was necessary before the sensor was quantified. As shown in Fig. 11, the ratios of vibration amplitudes over ac deflection voltages were given at different high dc voltages. The frequency of the deflection voltages, which was chosen bellow the natural frequency, was kept constant during the measurement. The ratio value at a dc bias of 50 V was marked as an asterisk because it was the intended working point thereafter.

Derived from the analysis above, The curve in Fig. 10 demonstrates the exponential relationship, verifying the electron tunneling effect. The semilog plot of tunneling current and displacement change is shown in Fig. 12, where the effective barrier height $\Phi = 0.1685$ eV was obtained according to Formula (1). The measured value is similar to the values in other groups [18], [28].

C. Closed-Loop Properties

Sensitivity of the tunneling accelerometer describes the property of the ability to transfer the acceleration into the electrical signal. In an open-loop system, the sensitivity is determined by the k/m ratio. In a closed-loop system, however, the sensitivity of the system is determined by the deep negative feedback factor, which was explained in [20]. Fig. 13 illustrates the sensitivity measurement result. In the plot, the output voltage increases linearly with the acceleration. However, the sensitivity, which is $20.6\,\mathrm{V/g}(1\mathrm{g} = 9.8\,\mathrm{ms}^{-2})$, can only be kept in linearity lower than 1.5 mg, 10% distortion from the linear relationship.

The sensitivity also changes at different frequencies in the working range. The sensitivities at different frequencies were measured when the input acceleration was kept the same. As shown in Fig. 14, the sensitivity is constant at low frequencies. When the frequency increases, there exists a cutoff frequency, after which the response decreases quickly. This cutoff frequency tells the system bandwidth of $B = 6.3$ kHz. B is larger than natural frequency f_o because the feedback system improved the stability, broadened the bandwidth, and reduced the fluctuation as described in [20].

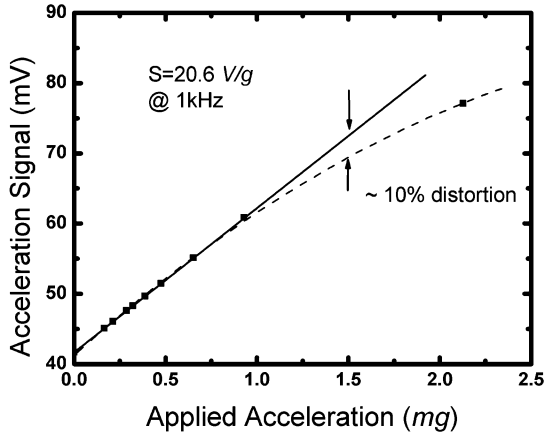

Fig. 13. The sensitivity of tunneling accelerometer. The plot describes the sensor ability to transfer the acceleration into the electrical signal. The linearity can be kept to 1.5 mg.

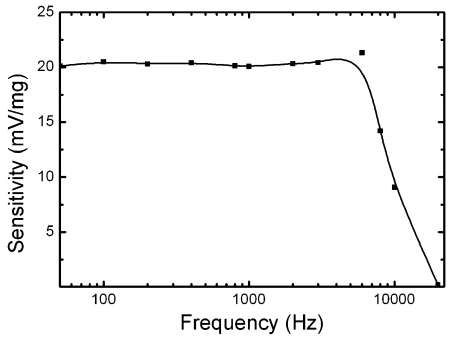

Fig. 14. The plot of micromachined accelerometer frequency ranges. The sensitivity is constant while the frequency increases to the cutoff frequency, $B = 6.3$ kHz.

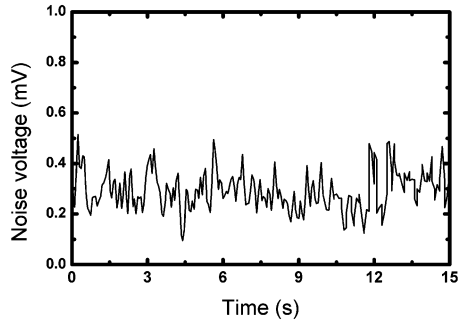

Fig. 15. The rms noise-time history record. After transferred to the input end, the noise level is calculated as 0.232 $\mu g/\sqrt{\text{Hz}}$.

D. Noise Measurement

The first way to measure noise level is to use Time History Record. The tunneling sensor was put in a quiet environment, where there was no force or acceleration. The accelerometers were set to zero, too. The fluctuation of deflection voltage was recorded in a period of time, as shown in Fig. 15. The recorded noise voltage V_{Nd} is a peak-to-peak value. The rms noise voltage is then equal to $V_N = (V_{Nd}/(2\sqrt{2}))$. After transferred to input end, the noise level is

$$\frac{V_N}{S} = \frac{\sqrt{\frac{(V_{Nd})^2}{8B}}}{S} = 0.232\ \frac{\mu g}{\sqrt{\text{Hz}}}$$

where S is the system sensitivity.

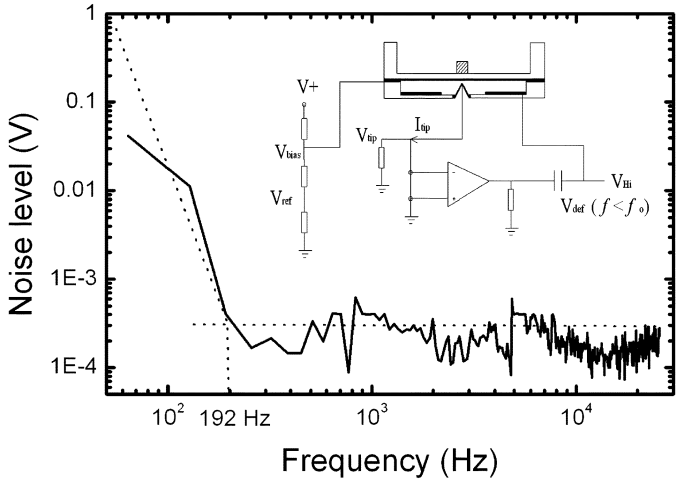

Fig. 16. The noise spectrum of the same tunneling sensor measured in Fig. 15. The noise behaves as a white noise at the frequencies higher than 192 Hz. The white noise level is 405 μV. At lower frequency, the noise increases quickly, which is the typical $1/f$ behavior. The noise resolution is 0.2485 $\mu g/\sqrt{\text{Hz}}$ at white noise level.

The second means that we used for noise spectrum was directly from PULSE analyzer 3560C. Fig. 16 describes the noise spectrum with the measurement circuit showed together. The noise of the same tunneling sensor behaves as white noise at the frequencies higher than 192 Hz and the white noise level is 405 μV. The noise is transferred into the input end, given by

$$N_a = \frac{V_N}{S} = \frac{\sqrt{\frac{(V_N)^2}{B}}}{S} = 0.2485\ \frac{\mu g}{\sqrt{\text{Hz}}}$$

where N_a is the acceleration resolution described as $g/\sqrt{\text{Hz}}$. The time history measurement and noise spectrum analysis give rise to the similar noise levels. At lower frequencies, the noise increases quickly, showing a $1/f$ behavior. Due to the dramatic noise increase at a low frequency, the PMMA accelerometer was not suitable for low frequency applications. A proper working frequency range should be 200 Hz–6.3 kHz.

The reason of noise sources is still an open question, though there are some concerns that the noise comes from thermal fluctuation of environment [16]. Grade *et al.* described temperature sensitive noise sources due to thermal expansion in metal-membrane bimorph structures and investigated low frequency noise spectrums in two modified structures [29]. The noise reduces were observed in metal-membrane-metal structure and a web electrode structure, even though the results were not conclusive.

VI. Conclusion

All-PMMA-based tunneling accelerometers have been successfully fabricated as the first demonstration of the PMMA tunneling sensor platform. Compared with the traditional silicon-based tunneling sensors, PMMA is less expensive, has less stiffness, and is easier to fabricate with the hot embossing micromachining process. Moreover, this all-PMMA-based tunneling sensor can be one of functional micro-sensors/devices for biomedical applications. The hot embossing technique, one of the most widely used micromachining approaches in

"soft-lithography," was chosen for its fast turnaround, less processing procedure, and simplicity. Because the mold can be used repeatedly, the potential of mass production is discussed in this work. Given all our research results, we can expect that the PMMA-based tunneling sensor platform will become the platform for the next generation of highly sensitive microsensors in many important areas, notably in magnetic, infrared, chemical, and biological applications.

ACKNOWLEDGMENT

The Authors thank Mr. J. Fang at the Institute for Micromanufacturing of Louisiana Tech University for the ICP processing.

REFERENCES

[1] C. F. Quate, "Tunneling accelerometer," *J. Microscopy*, vol. 152, pp. 73–76, 1988.
[2] S. B. Waltman and W. J. Kaiser, "An electron tunneling sensor," *Sensors and Actuators, A: Physical*, vol. 19, pp. 201–210, 1989.
[3] T. W. Kenny, S. B. Waltman, J. K. Reynolds, and W. J. Kaiser, "Micromachined silicon tunneling sensor for motion detection," *Appl. Phys. Lett.*, vol. 58, pp. 100–102, 1991.
[4] P. Scheeper, J. K. Reynolds, and T. W. Kenny, "Development of a modal analysis accelerometer based on a tunneling displacement transducer," in *Int. Conf. Solid-State Sensors and Actuators, Proc.*, vol. 2, 1997, pp. 867–870.
[5] R. L. Kubena, G. M. Atkinson, W. P. Robinson, and F. P. Stration, "A new miniaturized surface micromachined tunneling accelerometer," *IEEE Electron Device Lett.*, vol. 17, pp. 306–308, Jun. 1996.
[6] C. Yeh and K. Najafi, "A low-voltage bulk-silicon tunneling based accelerometer," in *Technical Digest, IEEE Int. Electron Devices Meeting (IEDM)*, Washington, DC, Dec. 1995, pp. 593–596.
[7] T. W. Kenny, W. J. Kaiser, S. B. Waltman, and J. K. Reynolds, "A novel infrared detector based on tunneling displacement transducer," *Appl. Phys. Lett.*, vol. 59, pp. 1820–1822, 1991.
[8] M. L. Hupert, M. A. Witek, Y. Wang, M. W. Mitchell, Y. Liu, Y. Bejat, D. Nikitopoulos, J. Goettert, M. C. Murphy, and S. A. Soper, "Polymer-based microfluidic devices for biomedical applications," *Proc. SPIE*, vol. 4982, pp. 52–64, 2003.
[9] L. J. Heyderman, C. Padeste, J. Gobrecht, and H. Schift, "Chemical nano-patterning using hot embossing lithography," *Microelectron. Eng.*, vol. 61–62, pp. 423–428, Jul. 2002.
[10] N. Keil, H. H. Yao, C. Zawadzki, J. Bauer, M. Bauer, C. Dreyer, and J. Schneider, "Athermal all-polymer arrayed-waveguide grating multiplexer," *Electron. Lett.*, vol. 37, no. 9, pp. 579–580, Apr. 2001.
[11] T. Ammer, M. T. Gale, and M. Rossi, "On-chip replication of micro-optical structures for VCSEL to fiber coupling," *Proc. SPIE*, vol. 4440, pp. 238–245, 2001.
[12] L. Lin, Y. T. Cheng, and C. J. Chiu, "Comparative study of hot embossed micro structures fabricated by laboratory and commercial environments," *Microsyst. Technol.*, vol. 4, no. 3, pp. 113–116, 1998.
[13] S. Y. Chou and P. R. Krauss, "Imprint lithography with sub-10 nm feature size and high throughput," *Microelectron. Eng.*, vol. 35, no. 1–4, pp. 237–241, 1997.
[14] C. H. Liu, J. D. Grade, A. M. Barzilai, J. K. Reynolds, A. Partridge, H. K. Rockstad, and T. W. Kenny, "Characterization of a high-sensitivity micromachined tunneling accelerometer source," in *Proc. Int. Conf. Solid-State Sensors and Actuators*, vol. 1, 1997, pp. 471–472.
[15] P. R. Scheeper, J. K. Reynolds, and T. W. Kenny, "Development of a modal analysis accelerometer based on a tunneling displacement transducer," in *Proc. Int. Conf. Solid-State Sensors and Actuators*, vol. 2, 1997, pp. 867–870.
[16] T. B. Gabrielson, "Mechanical-thermal noise in micromachined acoustic and vibration sensors," *IEEE Trans. Electron Devices*, vol. 40, pp. 903–908, 1993.
[17] C. H. Liu, H. K. Rockstad, and T. W. Kenny, "Robust controller de-sign via m-synthesis for high-performance micromachined tunneling accelerometers," in *Proc. 1999 American Control Conf.*, 1999, pp. 247–252.
[18] C. H. Liu and T. W. Kenny, "A high-Precision, wide-bandwidth micromachined tunneling accelerometer," *J. Microelectromech. Syst.*, vol. 10, pp. 425–433, Sep. 2001.
[19] A. Partridge, J. K. Reynolds, J. D. Grade, B. J. Kane, N. I. Maluf, G. T. A. Kovacs, and T. W. Kenny, "An integrated controller for tunnel sensors," *IEEE J. Solid-State Circuits*, vol. 34, pp. 1099–1107, 1999.
[20] J. Wang, Y. Zhao, T. Cui, and K. Varahramyan, "Synthesis of the modeling and control systems of a tunneling accelerometer using the MatLab simulation," *J. Micromech. Microeng.*, vol. 12, no. 6, pp. 730–735, Nov. 2002.
[21] T. W. Kenny and J. K. Reynolds, "Micromachined infrared sensors using tunneling displacement transducers," *Rev. Sci. Instrum.*, vol. 67, no. 1, pp. 112–128, Jan. 1996.
[22] B. Bhushan and X. Li, "Micromechanical and tribological characterization of doped single-crystal silicon and polysilicon films for microelectromechanical systems devices," *J. Mater. Res.*, vol. 12, no. 1, pp. 54–63, 1997.
[23] K. Howard, T. W. Kenny, J. K. Reynolds, W. J. Kaiser, T. R. VanZandt, and T. B. Gabrielson, "Miniature high-resolution accelerometer utilizing electron tunneling, Rockstad," *Amer. Soc. Mechan. Eng.*, vol. 40, pp. 41–52, 1992.
[24] P. G. Hartwell, F. M. Bertsch, S. A. Miller, K. L. Turner, and N. C. MacDonald, "Single mask lateral tunneling accelerometer," in *Proc. IEEE Micro Electro Mechanical Systems (MEMS)*, 1998, pp. 340–344.
[25] C. Yeh and K. Najafi, "Micromachined tunneling accelerometer with a low-voltage CMOS interface circuit," in *Proc. Int. Conf. Solid-State Sensors and Actuators*, vol. 2, 1997, pp. 1213–1216.
[26] W. J. Dauksher, S. B. Clemens, D. J. Resnick, K. H. Smith, P. J. S. Mangat, S. Rauf, P. Stout, P. L. G. Ventzek, H. J. Hopkins, and A. Chambers, "Modeling and experimental data using a new high rate ICP tool for dry etching 200 mm EPL masks. Microelectronic engineering," *Microelectron. Eng.*, vol. 61–62, pp. 887–894, Jul. 2002.
[27] M. A. Karabeyoglu and D. Altman, "Dynamic modeling of hybrid rocket combustion," *J. Prop. Power*, vol. 15, no. 4, pp. 562–571, 1999.
[28] C. H. Liu, A. M. Barzilai, J. K. Reynolds, A. Partridge, T. W. Kenny, J. D. Garde, and H. K. Rockstad, "Characterization of a high-sensitivity micromachined tunneling accelerometer with micro-g resolution," *J. Microelectromech. Syst.*, vol. 7, pp. 235–244, Jun. 1998.
[29] J. Grade, A. Barzilai, J. K. Reynolds, C. H. Liu, A. Partridge, L. M. Miller, J. A. Podosek, and T. Kenny, "Low frequency drift in tunneling sensors," in *Proc. Transducers' 97*, vol. 2, 1997, pp. 871–874.

Tianhong Cui (SM'00) received the B.S. degree from Nanjing University of Aeronautics and Astronautics in 1991, and the Ph.D. degree from the Chinese Academy of Sciences in 1995.

He is currently a Nelson Associate Professor of Mechanical Engineering at the University of Minnesota. From 1999 to 2003, he was an Assistant Professor of Electrical Engineering at Louisiana Technical University. Prior to that, he was a STA fellow at National Laboratory of Metrology, and served as a Postdoctoral Research Associate at the University of Minnesota and Tsinghua University. His current research interests include MEMS/ NEMS, nanotechnology, and polymer electronics.

Jing Wang received the B.S. and M.S. degrees in 1993 and 1996, respectively, all in electrical engineering from the Department of Electrical Engineering, Nankai University, Tianjin, China and the Ph.D. degree in Electrical Engineering from the Institute for Micromanufacturing, Louisiana Tech University, in 2003.

He is currently a Postdoctoral Fellow at the Department of Mechanical Engineering and Applied Mechanics (MEAM), University of Pennsylvania. From 1996 to 1999, he worked as a Research Engineer at the Institute of Physics, Chinese Academy of Sciences (CAS), Beijing, China. His research interests include microfabrication technologies, solid-state sensors and actuators, polymer microelectronics, μTAS, and bio-MEMS.